SITE CHARACTERIZATION REPORT
SHER: Hérémence (VS), Route du Solitaire

Paolo Bergamo, Mauro Häusler, Donat Fäh

Last modification: 14.10.2019

Contents

Summary

The new SSMNet station SHER was installed (20.7.2017) in the territory of the municipality of Hérémence (VS), at the hamlet of Le Melan. The station was purposely deployed in a peculiar geological setting, i.e. large-scale landslide (glissement des Masses) which is affecting an area of approximately 2 x 2 km on the western flank of the Val d'Hérens. Active seismic measurements, as well as a single-station noise recording survey, were performed to characterize the subsurface structure beneath the station. The site is characterized by a low fundamental frequency (0.77 Hz), which can be related to a deep interface between hard rock formations, well beyond the investigation depth reached by our measurements (which is approximately 60 m). The acquired H/V ratio curve presents as well a marked higher order peak at 4.77 Hz, which can be assigned to a horizon at around 35 m depth between the surficial layers of unconsolidated sediments (colluvium, landslide deposits) and the underlying quartz shale bedrock. This peak on the H/V curve corresponds to the most prominent peak (at 4.6 Hz) on the experimental Fourier amplification function derived from earthquake waveforms recorded at SHER. The estimated V_{S30} value is 464 m/s, which classifies the site as C type soil according to SIA261 (SIA, 2014), and as B following Eurocode 8 (CEN, 2004).

1.   Introduction.

In the framework of the second phase of the SSMNet (Swiss Strong Motion Network) renewal project, a new station, labelled as SHER, was installed on 20.07.2017 in the territory of the municipality of Hérémence (VS), at the hamlet of Le Melan (Figure 1). The host site is located on the western flank of the lower Val d'Hérens, at an altitude of 1490 meters above sea level. An active seismic survey and a single-station H/V$_{noise}$ measurement were carried out on 16.11.2017 to ensure the seismic characterization of the site.

Figure 1 – Geographical location of SHER station, on the western flank of the lower Val d'Hérens (© Swisstopo).

2.   Geological setting

The site hosting SHER is located within a wide instable area known as "glissement des Masses", covering approximately 2 x 2 km; the instability can reach depths of up to 100 m (BEG 2015). The velocity of the sliding mass can reach several cm/year. The sliding movement affects the local formations of sericitic quartz schists and carbonate-rich sericitic schists, which also blend with surficial sediments (moraine, fluvio-glacial deposits). The weathering layer at the site of SHER is identified as moraine deposits from the last glaciation (Swiss Geological Atlas; Figure 2). Downslope of SHER we find recent alluvial deposits; whereas to the north, west and south, the sericitic shists outcrop.
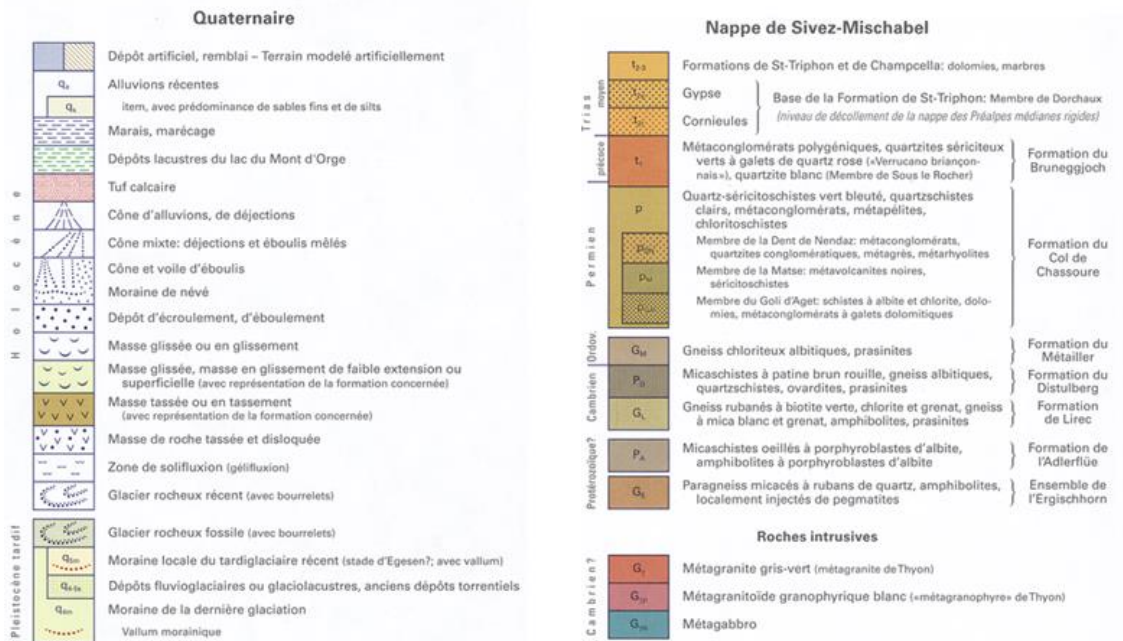
Figure 2 – Geological setting of SHER location, as illustrated by the Swiss Geological Atlas 1:25000 (Sheet 1306, Sion, © Swisstopo). The station rests on a formation of moraine of the last glaciation (light green), affected by compaction due to the action of the landslide.

Since the 1980s the area of the Heremence instability has been the object of several studies to assess the causes of the instability as well as its mechanisms (BEG, 2015). In particular, in the years 2011-2012 a series of seismic refraction tomography (SRT) lines were performed across the area (Geo2X, 2012), and several boreholes were drilled. Two of the seismic lines cross at a point few meters away

from the current position of SHER; at this location a borehole was dug (see Figure 3 for its position). The V_P sections from the SRT are unfortunately not available, however geological interpretations are reported in BEG (2015). For the SHER location, 29 m of sediments compacted by the landslide movement are reported. These rest on weathered bedrock, which is in turn replaced by compact rock at 50 m depth. The stratigraphic log of the borehole (see Figure 18, left) shows 2 meters of filling material at the top, 10 m of colluvium, 14 m of material displaced and compacted by the landslide, 6 meters of weathered bedrock followed by fresh rock (down to the bottom of the borehole 44 m below the soil surface).

3.   Active seismic measurements

The active seismic line was deployed few meters to the north-east of station SHER, along the side of a road (Figure 3).
For the sake of a comprehensive subsurface characterization, multichannel analysis of surface waves (MASW; Park et al., 1999) and P-wave refraction (Redpath, 1973) surveys were conducted.

3.1 Equipment

We used two sets of 8 three-component geophones (4.5 Hz corner frequency). Each geophone set was connected to a Geode datalogger; the two Geodes were coupled for time synchronization. The seismic source was a 5-kg sledgehammer, hitting a flat metal plate at nine source locations (yellow stars in Figure 3).
The synchronization between the traces recorded by the geophones and the seismic source was ensured by a trigger device fastened to the hammer handle.
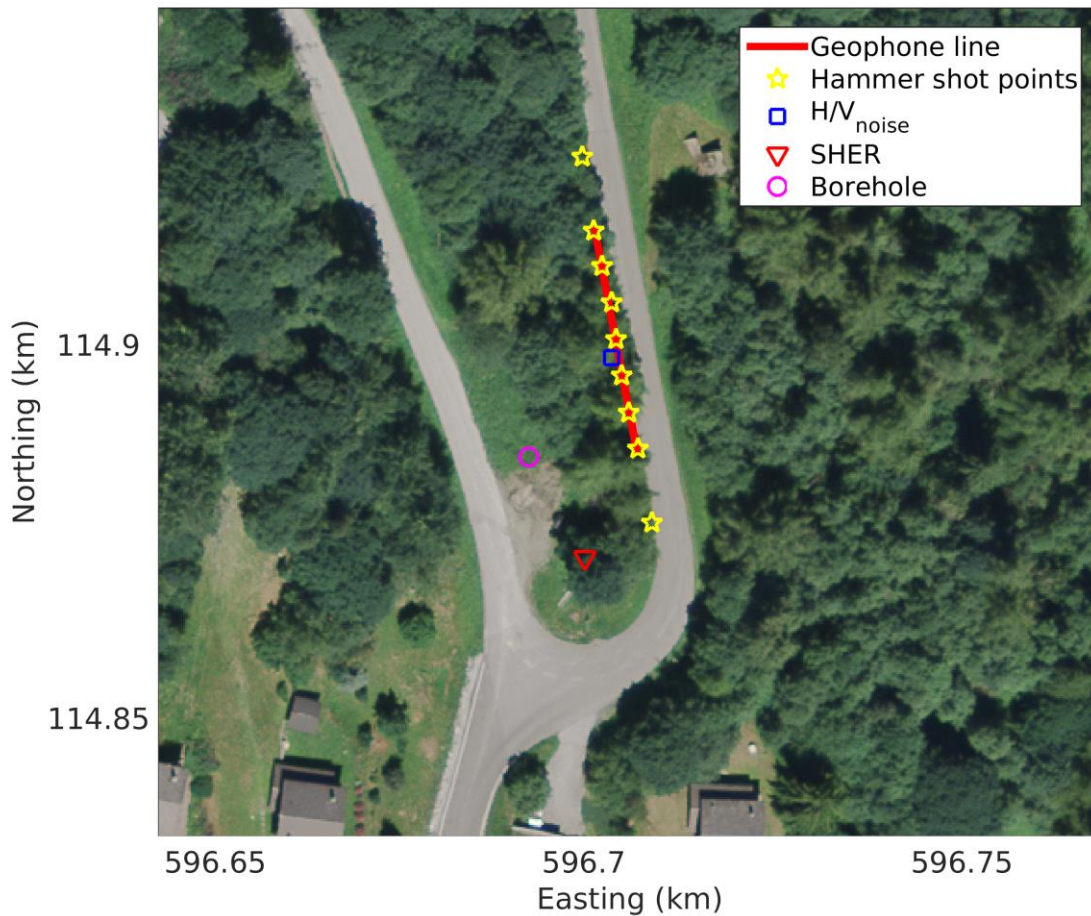
Figure 3 – Map representing the position of the targeted station (SHER, red triangle), of the active seismic line (red line and yellow stars), of the noise recording sensor (blue square), and of the nearby borehole (magenta circle).

3.2 Geometry of the acquisition array

The seismic line was constituted by 16 three-component receivers aligned at regular intervals of 2 m, for a total length of 30 m. The geophones were laid on the soil with metal spikes ensuring a firm coupling with the ground.

As earlier anticipated, MASW and P-wave refraction measurements were performed. As for the refraction survey, the sources were placed at seven locations along the receivers' line: at the south end, at 5 intermediate positions, and at the north end (Figure 3). Two additional MASW shooting positions were placed south and north of the array 10 m from the closest geophone (Figure 3).

Figure 4 – Geophone array in place. The picture was taken at the south end of the line.

3.3 Acquisition

The time-sampling parameters adopted for both MASW and refraction acquisitions were the following: sampling interval = 62.5 µs, record length = 1.5 s, pre-trigger delay = -0.05 s.

At the seismic refraction source points, 5 hammer shots were blown; the traces generated by each blow were iteratively stacked and finally saved in a single *.sg2* file.

As for the MASW acquisition, at each of the two shot points 10 hammer blows were repeated; the traces generated by each shot were separately saved in an *.sg2* file (without automatic stack).

In Figure 5 we show the seismic sections from a refraction (top) and a MASW (bottom) shot. P-wave first-break arrivals are clearly visible in the top subplots. In the bottom ones the Rayleigh wave wavetrain can be identified.
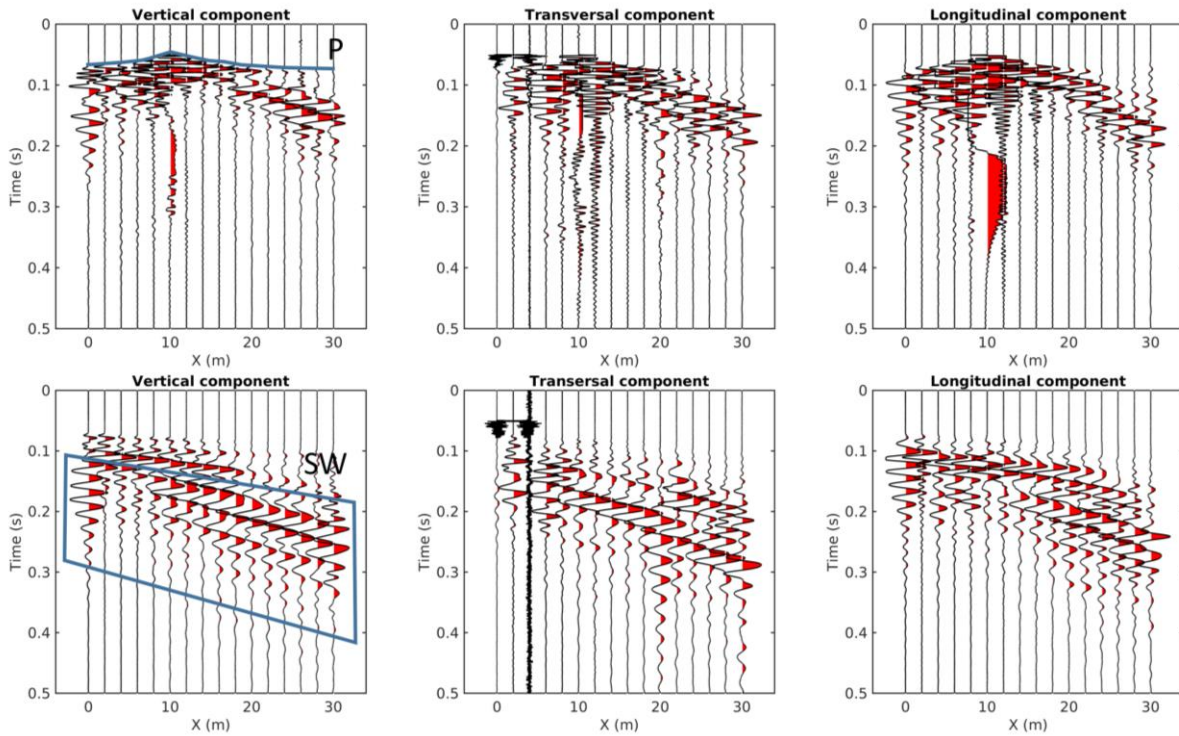
Figure 5 – Examples of acquired seismic sections. Top: traces from a refraction shot. P-wave first-break arrivals are highlighted with a blue line in the vertical component subplot. Bottom: traces from a MASW acquisition. The Rayleigh wave wavetrain is highlighted with a blue polygon in the vertical component subplot. The X coordinate in all subplots is the distance from the southernmost geophone.

3.4 Processing

3.4.1 Refraction processing

P-wave first-break arrival times were manually picked on the stacked seismograms representing the vertical component of soil surface vibration. For completeness P-wave arrivals were picked on the seismic sections from all available source positions (including also MASW shots). Figure 6 represents the travel-time curves, or hodocrones, obtained from each source position. The hodocrones appear to be approximately symmetrical, thus suggesting a 1D geometry (no lateral variations) for the near-surface below the active seismic array. The only exception is constituted by the long-offset arrivals from the hammer point at X = 40 m, which is anyway relatively far from the geophone line.
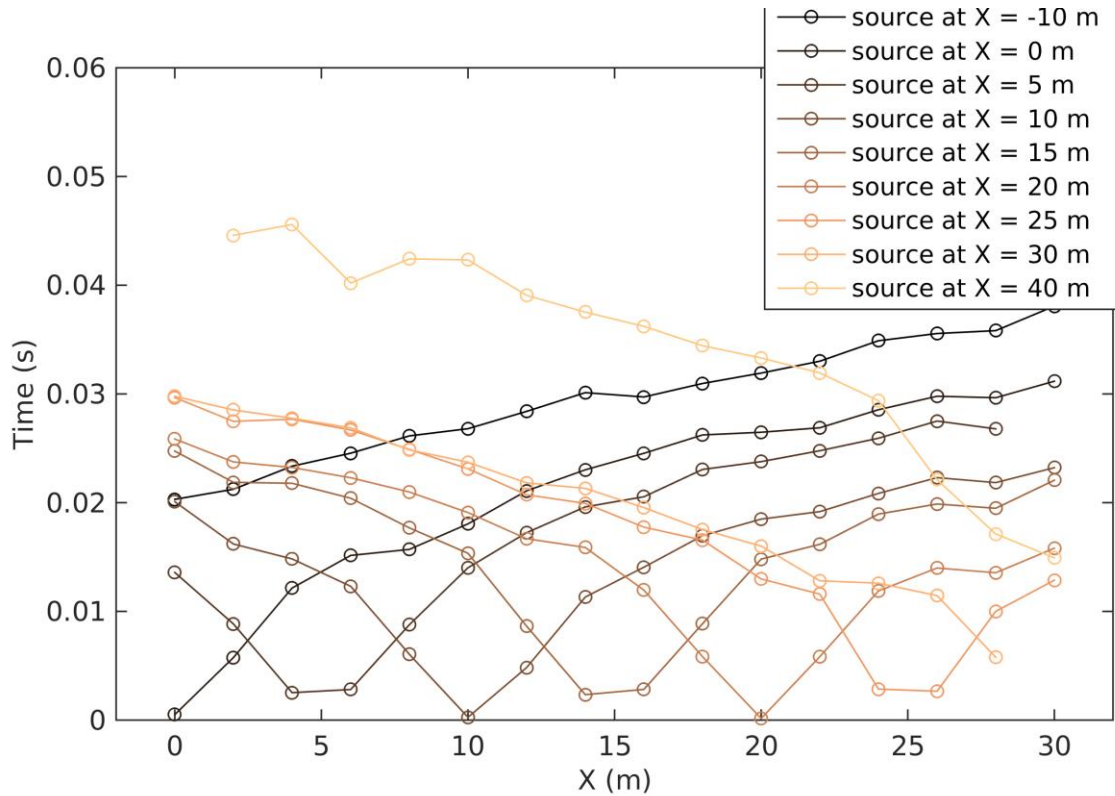
Figure 6 – P-wave refraction processing. Picked P-wave first-break arrival times from each shooting position. The X coordinate is the distance from the southernmost geophone.

3.4.2   Rayleigh wave data f-k processing

Rayleigh wave dispersion data were extracted from the vertical and radial component seismograms from MASW acquisitions. The considered seismic sections were processed by means of a 2D *f-k* (frequency – wavenumber) transform (Socco and Strobbia, 2004), in order to obtain a conversion of the recorded sets of traces from time–offset to frequency–wavenumber domain. *f-k* panels from single shot records with the same source position were summed to obtain spectral images with greater S/N ratio (O'Neill, 2003; Neducza, 2007). The energy maxima corresponding to the Rayleigh wave dispersion curves were picked on these stacked panels; spectral amplitude peaks from individual shot recordings were identified as well, and used to define the uncertainty intervals in the estimation of phase velocities (Socco et al., 2009; Boiero and Socco, 2010).

Figure 7 shows the stacked *f-k* panels from the considered seismic records, as well as the corresponding picked energy maxima. The dominant feature in all *f-k* spectra is a branch extending continuously in the 10-70 Hz frequency band, with wavenumbers between 0.1 and 1.5 rad/m. This feature is to be associated with the fundamental mode of Rayleigh wave propagation. At lower wavenumbers and higher frequencies other branches do exist and were picked. Their appearance is not necessarily coherent across all the four spectra, and they can be assigned to higher modes of surface wave propagation.
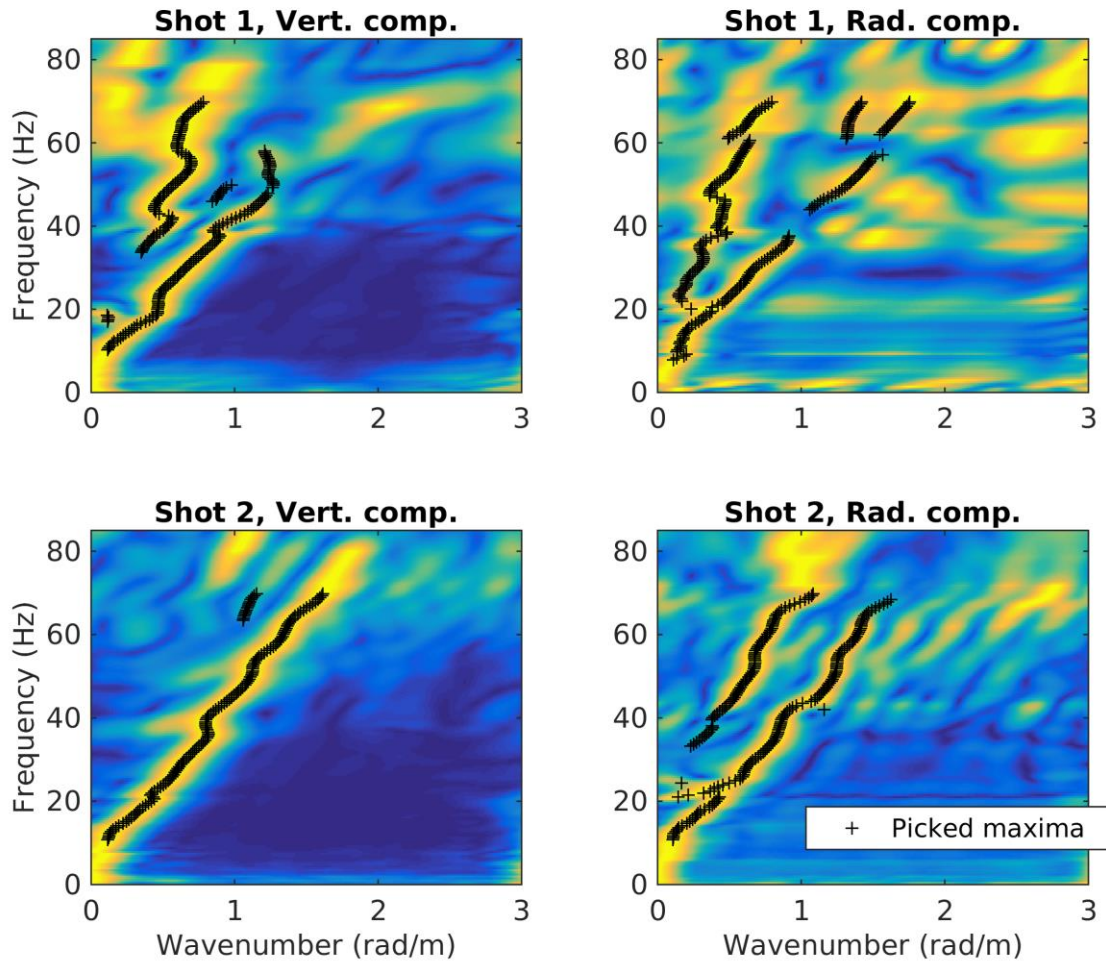
Figure 7 – Stacked normalized f-k spectra obtained from vertical and radial components of the seismic section with source positioned 10 m from the southernmost geophone (Shot 1), or 10 m from the northernmost receiver (Shot2). Black crosses are the picked energy maxima, corresponding to Rayleigh wave dispersion curve data points.

For a careful modal attribution of the picked branches we followed an approach inspired by the procedures proposed by Maraschini and Foti (2010) and Abdel Moati et al. (2013) and extensively described in the site characterization report of station SBIK (Bergamo et al., 2018).

The basic idea is to test the agreement between the experimental apparent dispersion curve and a set of synthetic curves corresponding to a vast population of possible subsurface models, assuming a priori only the reliable modal attribution of few data points, and letting the others free to be assigned to the closest (in terms of phase velocity) simulated mode. The synthetic curve that best "explains" (i.e. closely matches) all (or most of) the experimental data points, and therefore achieves the lowest misfit, is assumed to propose the most likely modal attribution.

The mode numbering resulting from this approach is shown in Figure 8. The fundamental mode of Rayleigh waves extends continuously across all the available frequency band (10 – 70 Hz) with velocities decreasing from 650 to 250 m/s. Above the fundamental mode sparser dispersive branches were attributed to modes from the 1st to 4th higher mode.
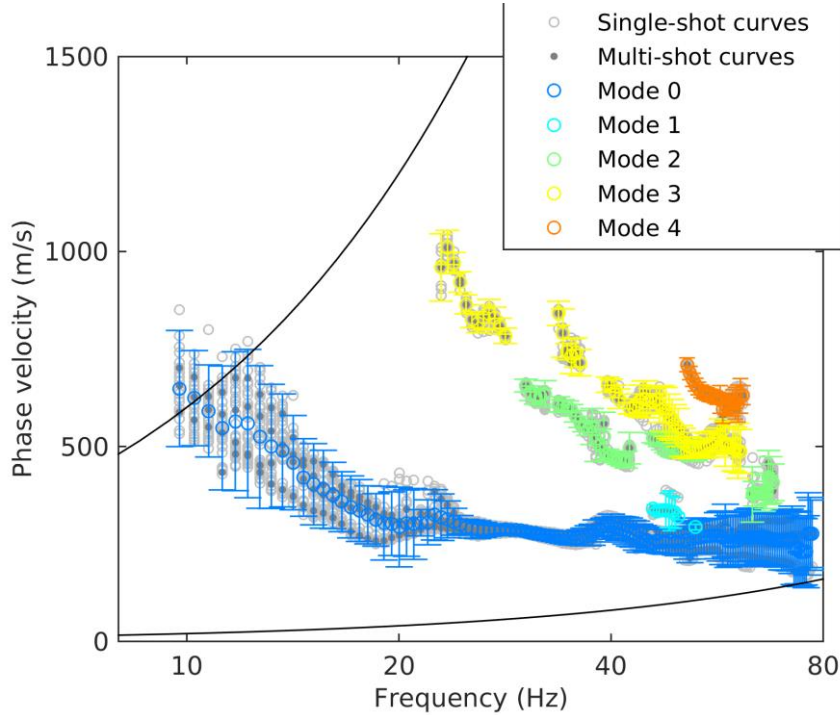
Figure 8 – Multimodal Rayleigh wave dispersion curve obtained from f-k processing. The dispersion curves from individual hammer blows (to be used for the estimation of the uncertainty intervals) are represented with gray circles. The dispersion curves picked on the four stacked f-k panels of Figure 7 are represented with gray dots; these curves were merged into a single, final curve, representative of the site (colored circles); the different colors refer to the identified modes; black lines represent the array resolution limits.

3.4.3   WaveDecActive

To retrieve the properties of Rayleigh wave propagation in terms of phase velocity and ellipticity the seismic traces acquired for the surface wave survey were also processed with the WaveDecActive code (Maranò et al., 2017). WaveDecActive implements a maximum likelihood algorithm for the analysis of Rayleigh waves generated by a controlled source. Key parameters required by WaveDecActive are the definition of the maximum number of Rayleigh waves that the code attempts to identify, and the value of parameter γ, which is able to modify the approach of the code towards wave identification from a Bayesian information criterion ($\gamma=1$) to a maximum likelihood approach (ML, $\gamma=0$) or a compromise between the two ($0<\gamma<1$). Following the recommendations of the code's author (Maranò, 2016) and some preliminary attempts, the maximum number of waves was set to 3 and γ to 0.2, thus opting for an approach close to a maximum likelihood solution.

The obtained results are displayed in Figure 9, showing the estimated Rayleigh wave phase velocities (left panel) and ellipticity angles (right panel) for the considered shots.
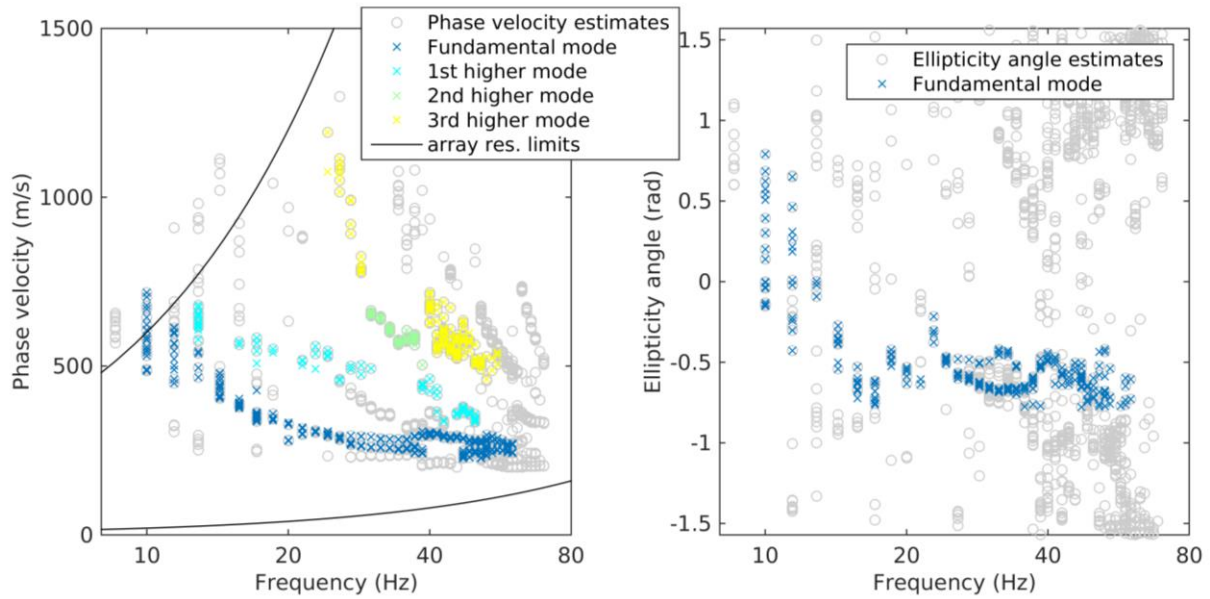
Figure 9 – Extraction of Rayleigh wave dispersion and ellipticity curve from WaveDecActive. Left: all estimated values of phase velocities (gray circles) and data points selected as belonging to the fundamental, 1ˢᵗ-3ʳᵈ higher mode of Rayleigh wave propagation (colored crosses). Right: all estimated values of ellipticity angle (gray circles) and data points selected as belonging to the fundamental mode of Rayleigh wave propagation (blue crosses).

In the phase velocity *vs* frequency panel data points were attributed to the various modes of Rayleigh wave propagation following the outcome of the mode numbering analysis described in the previous subsection. For the fundamental mode, we also retained the corresponding information regarding the angle of Rayleigh wave ellipticity (left panel in Figure 9). The ellipticity angle curve for the fundamental mode appears to be flat and around the negative value of -0.5 rad down to a frequency of 20 Hz, then it sharply increases to positive values with a zero-crossing at approximately 12 Hz.

4   Passive seismic measurement

4.1 Acquisition and equipment

Besides active seismic surveys, a single-station noise recording measurement was performed. A Lennartz 3C 5s seismometer connected to a Quanterra Q330 datalogger was deployed close to the midpoint of the geophone line (Figure 3). The sensor was placed on a metal tripod in a 10 cm deep hole for a better coupling with the ground (Figure 10). The sampling frequency was 200 Hz and the recording spanned a 45-minute time interval (before the active survey).

Figure 10 – Deployment of the Lennartz seismometer for microtremor recording.

4.2 Processing

The acquired passive traces were processed with the aim of:
- estimating the H/V ratio of recorded noise, thus identifying the fundamental frequency of resonance of the site (Nakamura, 1989) by the use of classical H/V methods (as implemented in Geopsy software, www. geopsy.org; classical H/V of Fäh et al., 2001).
- estimating the ellipticity of Rayleigh wave as a function of frequency by resorting to refined algorithms (Raydec, Hobiger at al., 2009; time-frequency method, Poggi and Fäh, 2010; wavelet-based time-frequency method as implemented in Geopsy software).

To obtain a more reliable estimation of Rayleigh wave ellipticity the latter methods aim at eliminating the contributions of other waves besides Rayleigh waves when compared to the classical H/V technique.

The results are shown in Figure 11. All applied techniques yield similar H/V or ellipticity curves with peaks at around 0.77 and 4.77 Hz and a deep trough at ~10 Hz. The frequency abscissa of the first peak at 0.77 Hz was identified as fundamental frequency.
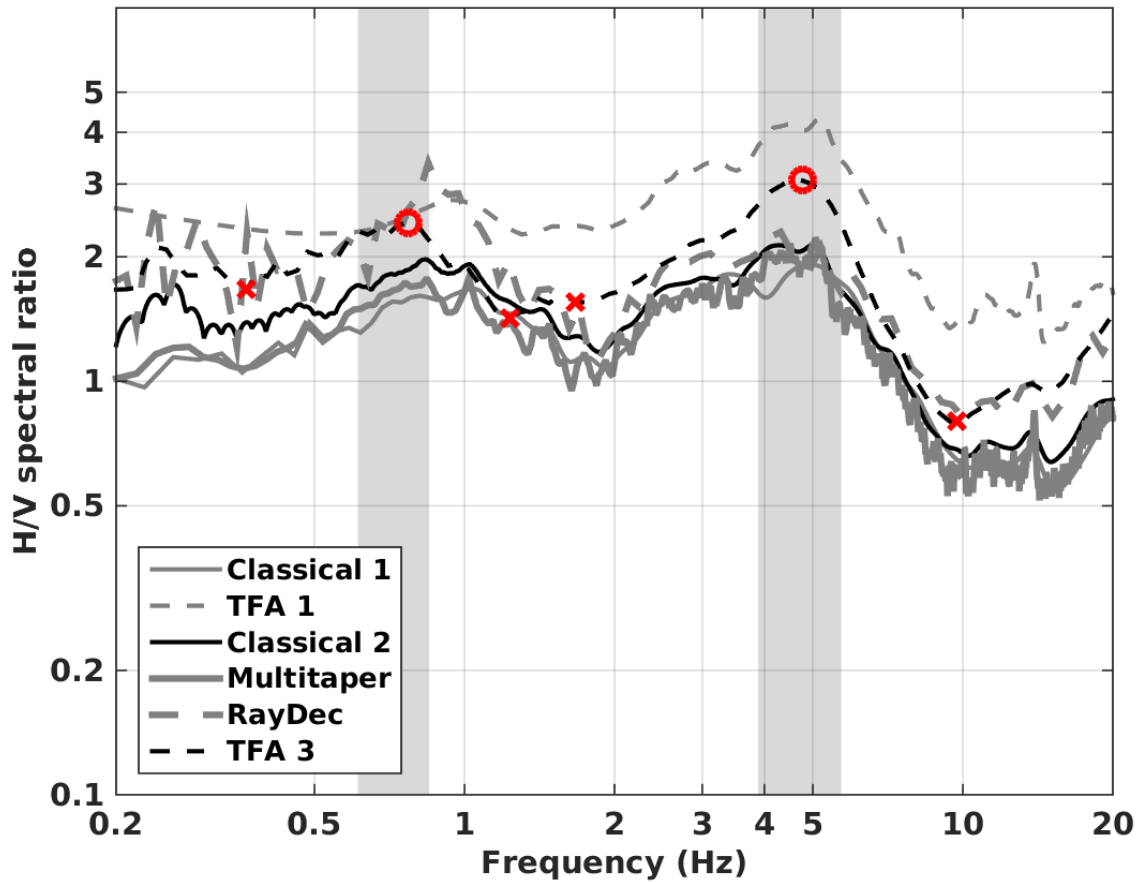
Figure 11 – H/V ratio and ellipticity curves obtained from the processing of noise recording data, using several algorithms. Classical 1: Geopsy; Classical 2: Fäh et al., 2001; TFA1: wavelet-based time-frequency method as implemented in Geopsy software; TFA3: time-frequency method, Poggi and Fäh, 2010; Raydec: Hobiger et al., 2009. Picked resonance frequencies are indicated by red circles; the corresponding intervals are marked by red crosses.

The recordings from the passive sensor were also processed with the polarization tool of Burjanek et al. (2010). In Figures 12 and 13 we display the produced ellipticity (as defined in Burjanek et al., 2010) and strike graphs as a function of frequency. The ellipticity plot (Figure 12) shows only a minor and a moderate trough at ~0.8 and 5 Hz, which correspond to the H/V peaks in Figure 11. For the polar strike (Figure 13) a weak directionality effect can be observed for the 5 Hz peak along the SW-NE axis, which is approximately the downslope direction at the sensor location. Since this peak does not reach high values of occurrence in the graph of Figure 13 we do not consider SHER as a site with predominant 2D resonance effects.
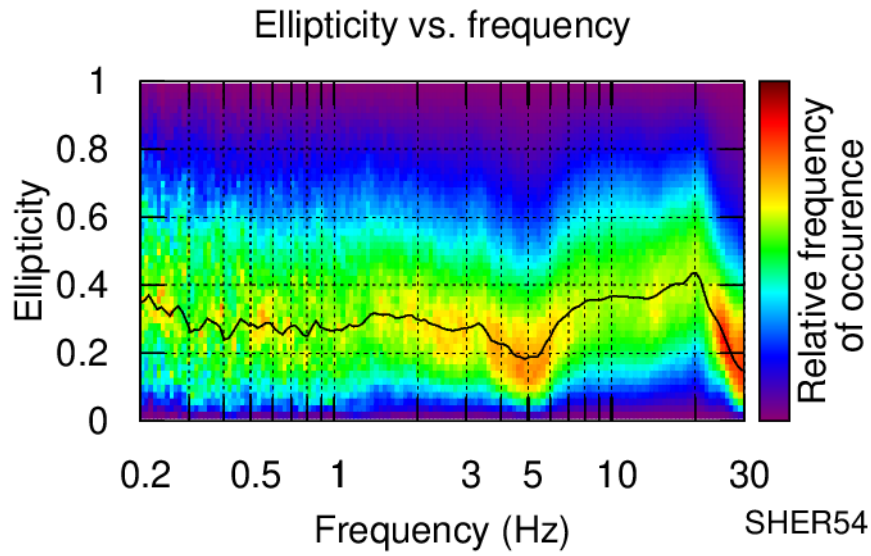
Figure 12 – Polarization analysis. Ellipticity vs frequency graph. The ellipticity is here intended as in Burjanek et al. (2010), i.e. the ratio between minor and major axes of the ellipse describing the instantaneous particle motion recorded at the soil surface.
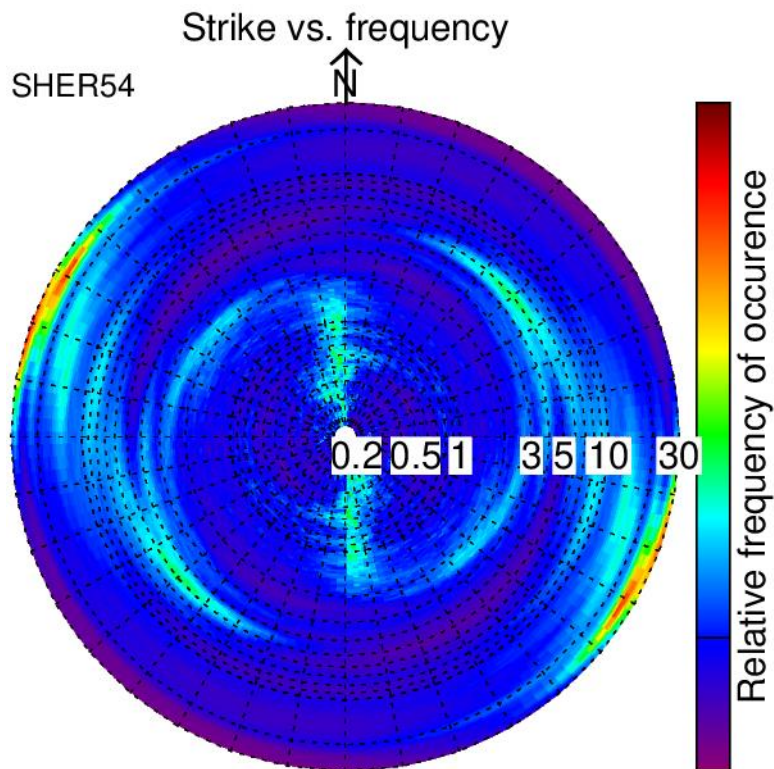

Figure 13 – Polarization analysis. Polar strike vs frequency graph.

5   P-wave travel-time inversion

A shallow V_P model of the subsurface was retrieved with the tomographic inversion of the picked P-wave arrival times (section 3.4.1). We used the seismic refraction tomography (SRT) inversion code developed at ETH Zurich by Lanz et al. (1998). The code performs a deterministic inversion of the arrival times. To minimize the distance between experimental and simulated arrival time a starting model is iteratively updated. For the inversion the 2D subsurface section below the active seismic array was modeled as a grid of 2 x 1 m cells. The initial model was defined as linear gradient of P-wave velocity with depth, increasing from 325 m/s at the surface with a rate of 220 m/s. A moderate constraint of spatial regularization was adopted.

The code converged to the final solution after 10 iterations, reaching a satisfactory fit with the experimental data (final RMSerror = 1.81 ms). From the analysis of the ray-paths at the last iteration (Figure 14, bottom), it is evident that the portion of 2D section with a sufficient ray coverage (i.e. constrained by input data) is the central area just below the geophone spread. It covers a maximum depth of approximately 10 m. This portion of the 2D section is the final result of the inversion process (Figure 14, top).

As shown in Figure 14 no sharp lateral variations are encountered and the velocity horizons are approximately parallel to the soil surface. In the shallow 3 meters V_P is around 700 m/s; the velocity then smoothly increases to ~1200 m/s between 3-6 m depth; below 6 m the velocity gradient is steeper and V_P is approximately 1900-2000 m/s at the maximum depth of investigation (~9 m).
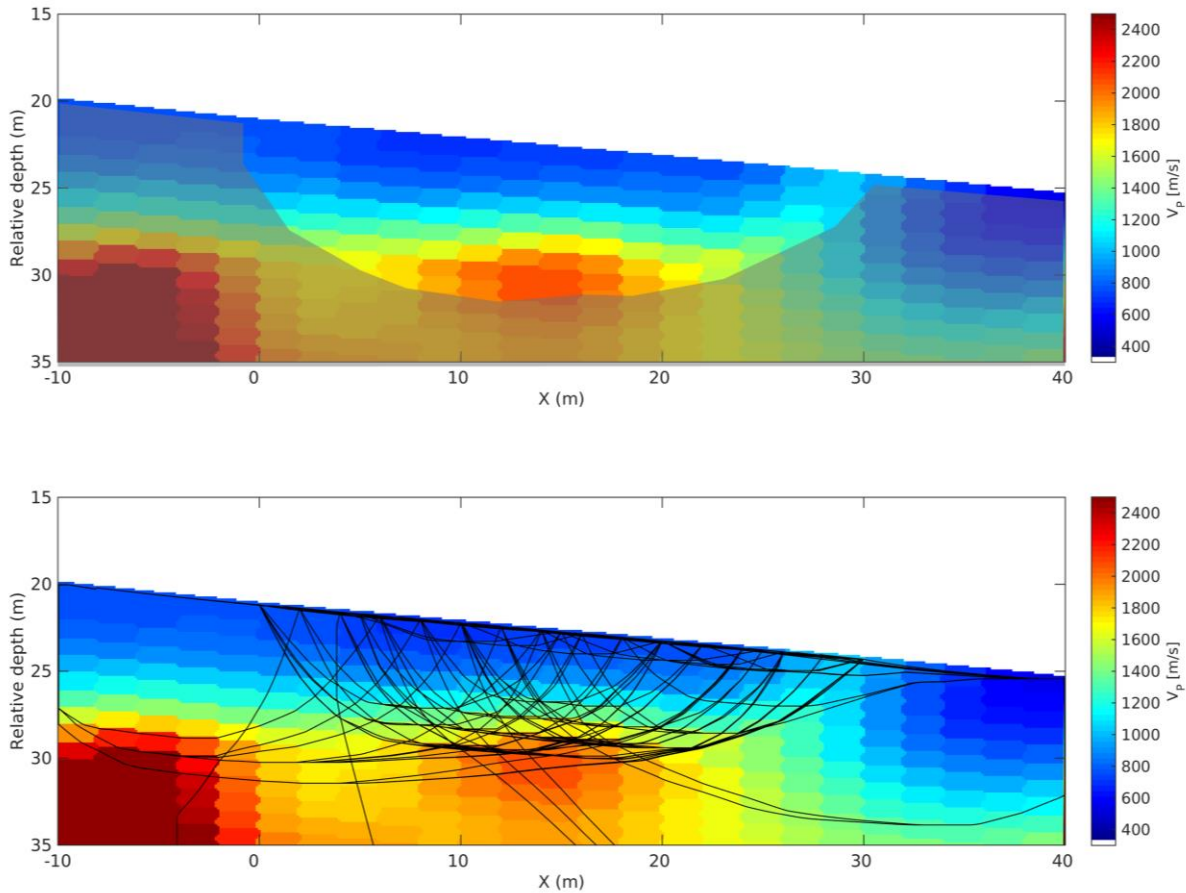
Figure 14 – tomographic inversion of P-wave first-break arrival times. Top: 2D V$_P$ section at the last iteration; the areas without insufficient or null ray coverage are shadowed in gray. Bottom: same as above, with the superposition of the modeled ray paths at the last iteration.

6   Inversion of Rayleigh wave data

The Rayleigh wave dispersion and ellipticity curves obtained from the processing of active and passive seismic data (see section 3.4) were inverted for the 1D S-wave velocity profile of the investigated site. For the inversion an ad-hoc code implemented in Matlab® was used. The code performs a Monte Carlo inversion, first generating a population of possible joint V$_S$/V$_P$ profiles, then computing the synthetic curves corresponding to each model, and finally evaluating the misfit with respect to the experimental curves. For the solution of the forward problem we resorted to Hermann (2013).

6.1 Inversion target

The target we selected for the inversion consists of:
- The multimodal Rayleigh wave dispersion curve, as obtained from the processing of active data with the WaveDecActive code (section 3.4.3; see Figure 15 left).

18

- The Rayleigh wave ellipticity curve for the fundamental mode from the processing of active data with WaveDecActive code, translated from ellipticity angle (Figure 9) to the ratio between horizontal and vertical component of particle motion (ellipticity).

At low frequency (< 10 Hz), this curve was joined with the ellipticity curve obtained from the single-station passive recording processed with Raydec (see section 4.2). This curve was attributed to the fundamental mode of Rayleigh wave propagation. To include the ~4.8 Hz peak we used data points from 10 down to 2 Hz for the inversion. The portion below 2 Hz was discarded as it is not accompanied by any information about Rayleigh wave phase velocity (the dispersion curve extends down to 10 Hz only).

The peak at 4.8 Hz and the through at 11 Hz in the ellipticity curve were cropped to allow the modelling of singularities at those frequencies (Hobiger et al., 2013; see Figure 15 right panel). The phase velocity and ellipticity curves were resampled on a logarithmically-spaced frequency vector with 100 elements between 2 and 60 Hz.
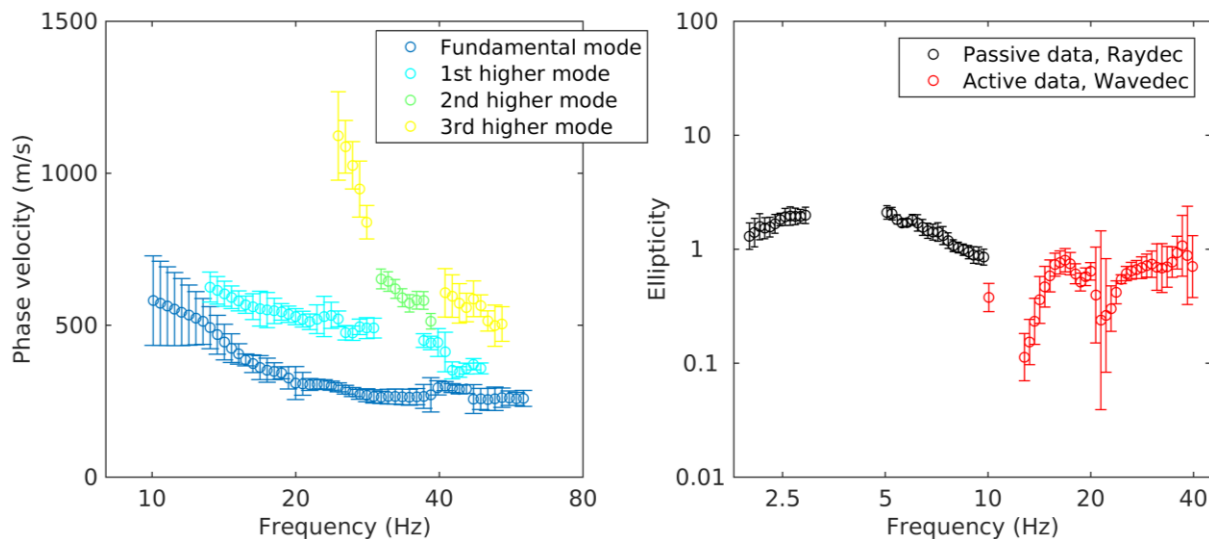

Figure 15 – Target of the Rayleigh wave data inversion process. Left: multimodal Rayleigh wave dispersion curve obtained from the processing of active data with WaveDecActive code. Right: ellipticity curve for the fundamental mode of Rayleigh wave; the low-frequency portion was obtained by processing passive data with Raydec code; the high-frequency portion was obtained from the processing of active data with Wavedec code.

6.2 Parameterization of the model space

For the parameterization of the subsurface model two different strategies were followed: the soil column was modelled as a stack of either 6 or 5 homogeneous layers with variable thickness + halfspace. In both parameterizations at each layer the V_S can vary within broad Monte Carlo boundaries. The same applies to V_P, although the resulting V_S/V_P ratio must be compatible with a range of possible values of Poisson's ratios set for each layer:

0.2 – 0.4 for the two shallowest formations, 0.2 – 0.49 for the following intermediate layers (to allow for the presence of water-saturated materials, as indicated by the SRT results, Figure 14), and 0.2 – 0.35 for the lower halfspace. Bulk density values are attributed to each layer increasing from 1.9 t/m^3 for the weathering formation to 2.2 t/m^3 for the halfspace. For the three deepest layers S-wave velocity values are forced to be larger than that of the formation above.

For each parameterization we completed an inversion run with 10^6 randomly generated models.

6.2 Inversion results

In Figures 16 and 17 we show the results obtained from each of the two inversion runs: Figure 16 with 6 layers + halfspace parameterization and Figure 17 with 5 layers + halfspace parameterization. The velocity profiles resemble each other. The 5-layer parametrization yields lower misfit values (minimum RMSE = 1.23, compared to RMSE = 1.44 for the 6-layer models). In the first case however the majority of best performing profiles fails to produce a fundamental mode ellipticity curve with a singularity at around 10 Hz. We believe that this feature is clearly indicated in our experimental data (see Figure 9). Therefore, we consider the models from the 6-layer parameterization as closer to the collected experimental information and we regard them as the final inversion result.
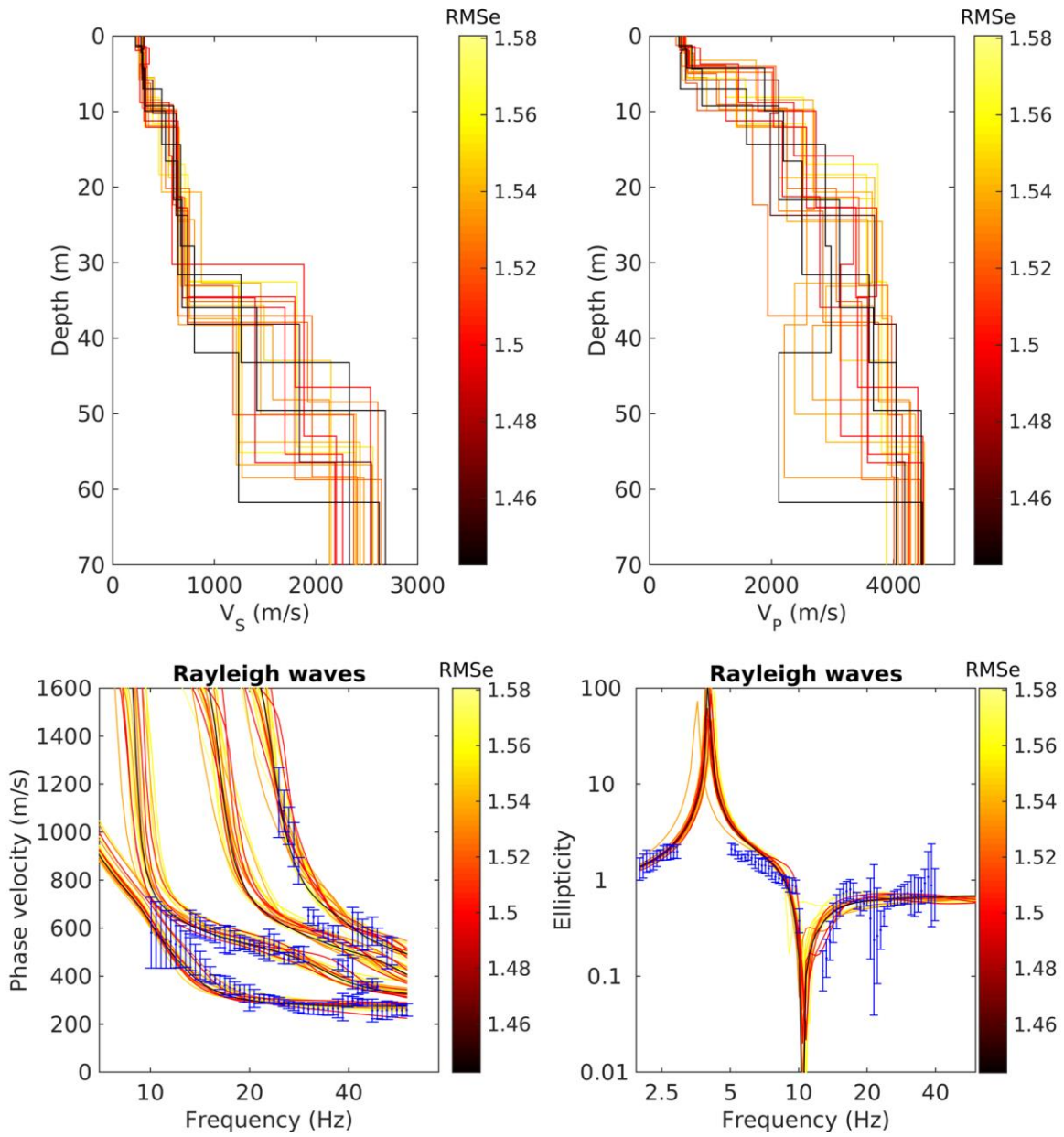
Figure 16 – 20 best performing models obtained from the 6-layer parameterization inversion run. Top: Vs and Vp profiles; bottom; fit of experimental Rayleigh wave dispersion curve and ellipticity curve with simulated curves.
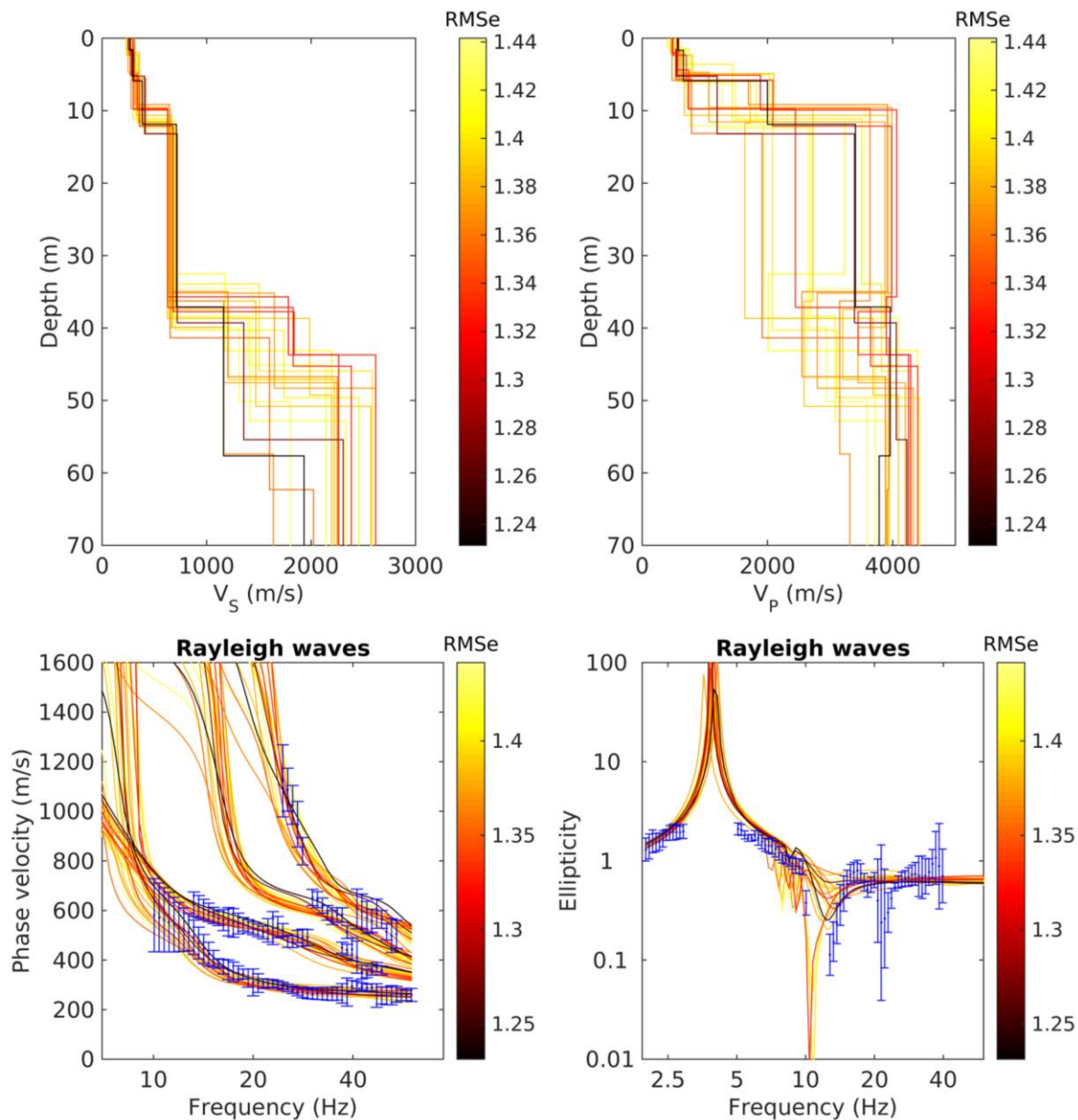
Figure 17 – 20 best performing models obtained from the 5-layer parameterization inversion run. Top: Vs and Vp profiles; bottom; fit of experimental Rayleigh wave dispersion curve and ellipticity curve with simulated curves.

7   Interpretation of the velocity profiles

7.1 Velocity profiles

The 20 best performing models from the 6-layer parametrization inversion are considered as final result. In Figure 18 their shallower portion (0 – 45 m) is compared to the stratigraphic profile from the nearby borehole (see Figure 3 for its location). The upper 10 m have a Vs around 300 m/s. According to the borehole they should be composed of colluvium. At approximately 10 m depth S-wave velocity sharply increases to ~600 m/s. Then it gradually increases to 700 m/s at around 35 m depth. From borehole data for this depth interval sedimentary material compacted by the landslide is

reported. This section is underlain by fractured rock blocks. The interface in the velocity profiles at ~35 m depth corresponds to the upper boundary of the weathered bedrock, which has an S-wave velocity of around 1500 m/s. The lower interface of this layer is placed by the velocity profiles at around 55 m depth (Figure 19), where the V_S increases to 2100-2500 m/s (quite likely fresh bedrock). We remark that the retrieved velocity profiles have a good agreement not only with the stratigraphic profile of Figure 18, but also with the geological model derived from the seismic surveys of Geo2X (2012) and reported in BEG (2015).
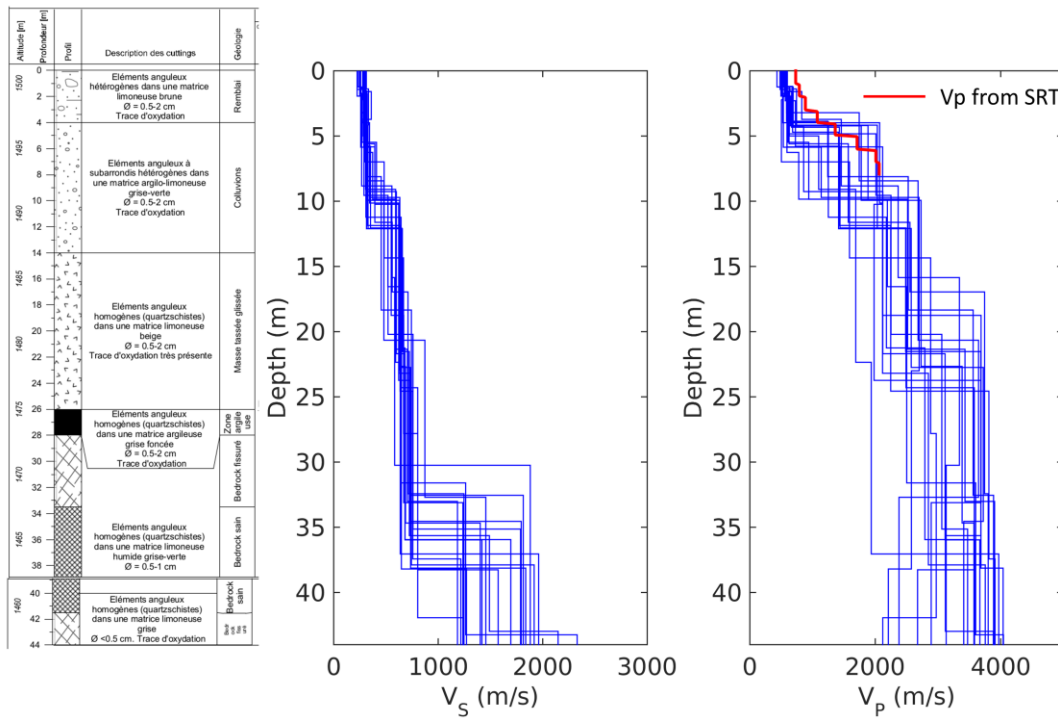

Figure 18 – Left: stratigraphic log from a nearby borehole (see Figure 3 for its location). Right: shallower portion (upper 45 m) of the obtained V_S and V_P profiles. In the rightmost panel the P-wave velocities at the midpoint of the retrieved SRT section (Figure 14) are shown (red line).
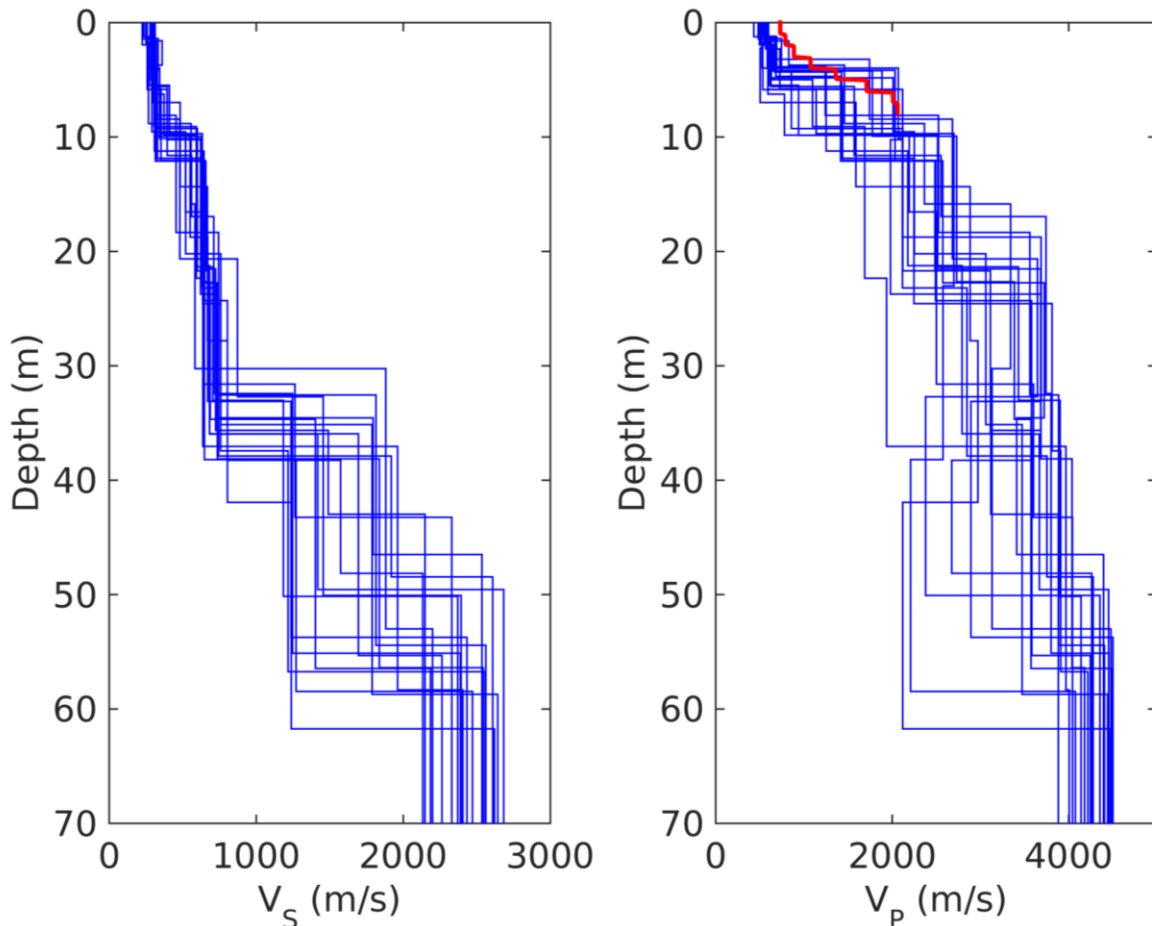
Figure 19 – Entire V$_S$ (left) and V$_P$ (right) profiles. In the right panel the P-wave velocities at the midpoint of the retrieved SRT section (Figure 14) are shown (red line).

7.2 Quarter-wavelength representation

The quarter-wavelength velocity representation (V$_S^{QWL}$; Joyner et al., 1981) attributes the average velocity at a depth equal to ¼ of the corresponding wavelength to each frequency. V$_S^{QWL}$ can be used as direct proxy for the local site characterization, as it physically relates the resolution on ground parameters with the characteristics of the propagating wave-field at the discrete frequencies. The derived quarter-wavelength impedance contrast (IC^{QWL}; Poggi et al., 2012) is the ratio between two quarter-wavelength average velocities from the top and bottom part of the velocity profile at a given frequency. It is a powerful tool to assess the influence of resonance phenomena in soft sediment sites. Figure 20 shows the average (over the population of the selected 20 best subsurface models) quarter-wavelength velocity (Figure 20 centre) and impedance contrast (Figure 20 bottom) representations. The obtained Vs30 (which is the average velocity corresponding to a quarter-wavelength of 30 m) is 464 m/s.

The IC^{QWL} graph shows one peak at 3.5 Hz, which can be associated with the impedance contrast between unconsolidated sediments and bedrock at 35 m depth (Figure 19).
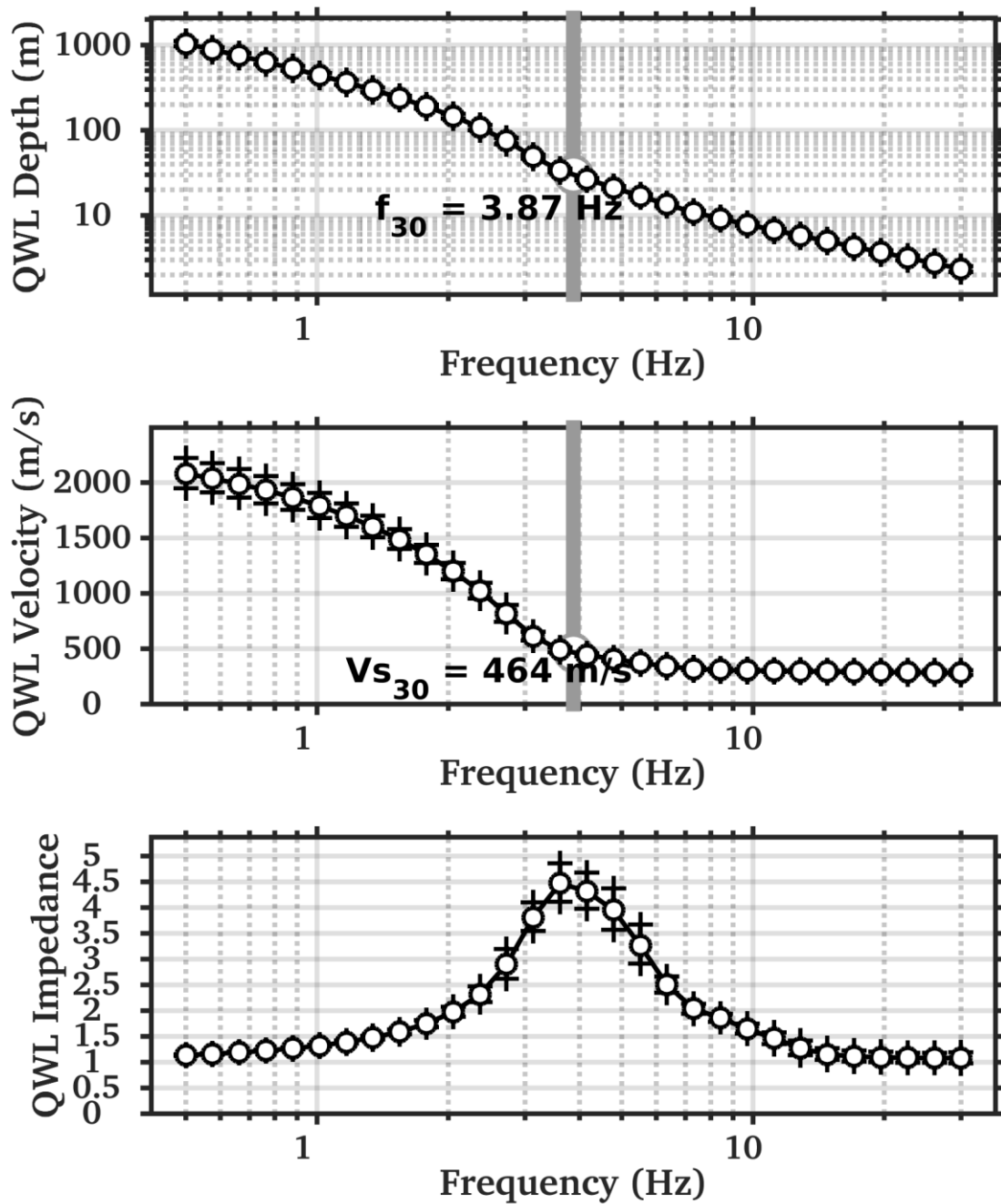
Figure 20 – Average quarter-wavelength representation of the selected velocity profiles (Figure 19). Top: depth; center: velocity; bottom: impedance contrast. The gray line in the top and center panel refers to Vs30.

7.3 SH transfer function.

The theoretical SH-wave transfer function for vertical propagation (Roesset, 1970) was computed for the selected models (Figure 21). The transfer functions were also corrected for the Swiss reference rock model (Poggi et al., 2011) following Edwards et al. (2013).

These are compared with the empirical amplification function obtained from spectral modeling (ESM; Edwards et al., 2013). The latter relies on 47 events in the 2.5 – 10 Hz frequency band and on ~ 10 events at lower and higher frequencies (as of 16.10.2019). The agreement between simulated and empirical amplification functions is relatively good. The first and main peak of the empirical amplification function at 4.6 Hz is reproduced by all synthetic curves; this peak is related to the impedance contrast between unconsolidated sediments and weathered bedrock at 35 m depth. The synthetic curves define also another peak at 9.5 Hz, to be assigned to the sudden velocity increase at ~ 10 m depth in the obtained velocity profiles (Figure 18): this feature appears to have no match in the empirical amplification function, although here a minor peak at 7.3 Hz is present.
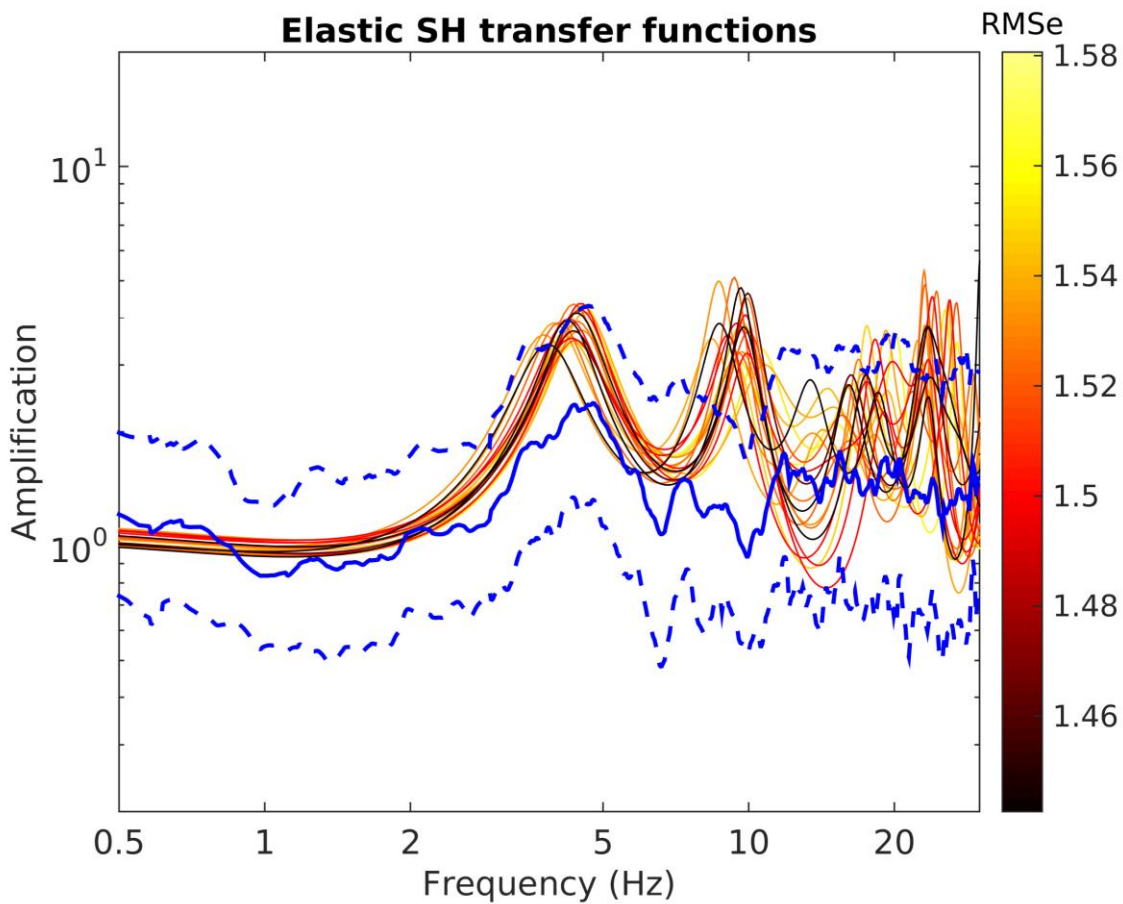

Figure 21 – Modeled SH transfer functions (colored lines) from the selected velocity profiles corrected for the Swiss reference rock model and compared with the empirical amplification function for SHER (blue line, uncertainty intervals in blue dashed line).

8   Conclusions

Active seismic measurements and a single-station noise recording were performed to characterize the structure of the subsurface below the SSMNet station SHER (Hérémence, VS). Active data were processed to derive Rayleigh wave dispersion, ellipticity curves and to identify the first-break arrivals of P-waves (later inverted with a tomographic approach). Passive data were analyzed to estimate the

ellipticity curve of Rayleigh waves. Rayleigh wave dispersion and ellipticity curves were inverted for the S-wave velocity profile at the station location.

The surficial 10 meters have a V_S around 300 m/s and should be composed of colluvium. At approximately 10 m depth, S-wave velocity sharply jumps to ~600 m/s. At around 35 m depth it gradually increases reaching 700 m/s. In this depth interval a nearby borehole reports uncemented material compacted by the landslide, underlain by fractured rock blocks. The interface in the velocity profile at ~35 m depth corresponds to the upper boundary of the weathered bedrock with an S-wave velocity of around 1500 m/s. The lower interface of this layer is located at around 55 m depth , where the V_S increases to 2100-2500 m/s in the velocity profiles (quite likely fresh bedrock).
The sharp velocity contrast at around 35 m depth is caused by the interface between unconsolidated sediments and weathered bedrock, and is responsible for the main peak of the experimental Fourier amplification function at 4.6 Hz and can also be associated to the f_1 peak in the H/V curve at 4.77 Hz.

The fundamental frequency (f_0) of the site is 0.77 Hz and was identified on the H/V curve. It is probably associated to an impedance contrast at a depth well beyond the investigation depth achieved by our measurements (around 60 m).

The estimated V_{S30} value is 464 m/s, which classifies the site as C type soils according to SIA261 (SIA, 2014) and as B following Eurocode 8 (CEN, 2004). The engineering bedrock (H800) is at approximately 35 m depth.

References

Abdel Moati W.H., D. Boiero, and L.V. Socco, 2013. A tool for fast underground characterization for trenchless pipeline construction by horizontal directional drilling technology. 11th Offshore Mediterranean Conference and Exhibition, Ravenna, Italy, March 20-22 2013.

BEG, Bureau d'Etudes Géologiques, 2015. Etude de projet "Glissement des Masses" rapport géologique. Rapport No/réf.:4370.

Bergamo P., M. Hobiger and D. Fäh, 2018. Site characterization report, SBIK – Biel/Bienne (BE), Kongresshaus/Palais des Congrès. Swiss seismological service (SED)

Boiero, D., and L. V. Socco, 2010. Retrieving lateral variations from surface wave dispersion curves analysis: Geophysical Prospecting, **58**, 977–996

Burjanek J., G. Gassner-Stamm, V. Poggi, J.R. Moore and D. Fäh, 2010. Ambient vibration analysis of an unstable mountain slope, GJI, 180, 820-828.

CEN, 2004. Eurocode 8: Design of structures for earthquake resistance – Part 1: general rules, seismic actions and rules for buildings. European Committee for Standardization, en 1998-1 edition.

Edwards, B., Michel, C., Poggi, V., and Fäh, D., 2013. Determination of Site Amplification from Regional Seismicity: Application to the Swiss National Seismic Networks. Seismological Research Letters, 84(4).

Fäh, D., F. Kind, and D. Giardini, 2001. A theoretical investigation of average H/V ratios. GJI, 145, no. 2, 535-549.

Geo2x sarl, 2012. Etude géophysique par sismique de la région d'Hérémence.

Herrmann, R. B., 2013. Computer programs in seismology: An evolving tool for instruction and research, Seism. Res. Lettr. **84**, 1081-1088, doi:10.1785/0220110096

Hobiger, M., C. Cornou, M. Wathelet, G. Di Giulio, B. Knapmeyer-Endrun, F. Renalier, P.Y. Bard, A. Savvaidis, S. Hailemikael, N. Le Bihan, M. Ohrnberger, and N. Theodoulidis, 2013. Ground structure imaging by inversion of Rayleigh wave ellipticity: sensitivity analysis and application to European strong motion sites. GJI, 192, 207-229.

Hobiger, M., P.-Y. Bard, C. Cornou, and N. Le Bihan, 2009. Single station determination of Rayleigh wave ellipticity by using the random decrement technique (Raydec). GRL, 36, L14303

Joyner, W. B., Warrick, R. E., and Fumal, T. E., 1981. The effect of Quaternary alluvium on strong ground motion in the Coyote Lake, California, earthquake of 1979. Bulletin of the Seismological Society of America, 71(4):1333–1349.

Lanz E., H. Maurer and A. G. Green, 1998. Refraction tomography over a buried waste disposal site. Geophysics, 63 (4), 1414-1433.

Marano' S., 2016. http://mercalli.ethz.ch/~marra/WaveDec/userguide_WaveDec.html

Marano, S., Hobiger M., P. Bergamo and D. Fäh, 2017. Analysis of Rayleigh Waves with Circular Wavefront: a Maximum Likelihood Approach. GJI, 210, 1570-1580.

Maraschini M., and S. Foti, 2010. A Monte Carlo multimodal inversion of surface waves. GJI, 182 (3). 1557 – 1566.

Neducza, B., 2007, Stacking of surface waves: Geophysics, 72, 51–58.

O'Neill, A., 2003, Full-waveform reflectivity for modelling, inversion and appraisal of seismic surface wave dispersion in shallow site investigations: PhD thesis, University of Western Australia, Perth, Australia.

Park, C. B., R. D. Miller, and J. Xia, 1999. Multichannel analysis of surface waves: Geophysics, **64**, 800–808.

Poggi, V., B. Edwards and D. Fäh, 2011. Derivation of a Reference Shear-Wave Velocity model from Empirical Site Amplification. BSSA, 101, no. 1, pp. 258-274

Poggi, V., B. Edwards and D. Fäh, 2012. The quarter-wavelength average velocity: a review of some past and recent application developments. 15th WCEE, Lisbon 2012.

Poggi, V., and D. Fäh, 2010. Estimating Rayleigh wave particle motion from three component array analysis of ambient vibrations. GJI, 180, no. 1, 251-267.

Redpath, B. B., 1973. Seismic refraction exploration for engineering site investigations: National Technical Information Service, Technical Report E-73-4.

SIA, 2014. SIA 261 Einwirkungen auf Tragwerke. Société Suisse des ingénieurs at des architectes, Zurich, Switzerland.

Socco, L.V., and C. Strobbia, 2004. Surface-wave method for near-surface characterization: a tutorial: Near Surface Geophysics, **2**, no. 4, 165-185.

Socco, L.V., D. Boiero, S. Foti, and R. Wisen, 2009. Laterally constrained inversion of ground roll from seismic reflection records: Geophysics, **74**, no. 6, G35-G45.

Swisstopo, Service géologique national, 2011. Atlas géologiques de la Suisse 1:25000 : 1306 feuille de Sion